International Journal of Hydrogen Energy 58 (2024) 1673–1681

Contents lists available at ScienceDirect

International Journal of Hydrogen Energy

journal homepage: www.elsevier.com/locate/he

A small angle X-ray scattering approach for investigating fuel cell catalyst degradation for both *ex situ* and *in operando* analyses

Marco Bogar [a,*], Yurii Yakovlev [b,**], Jaroslava Nováková [b], Alina Madalina Darabut [b], Manfred Kriechbaum [c], Heinz Amenitsch [c], Rodolfo Taccani [a], Iva Matolínová [b]

[a] Department of Engineering and Architecture, University of Trieste, Via Alfonso Valerio 6/1, 34127, Trieste, Italy
[b] Faculty of Mathematics and Physics, Charles University, V Holešovičkách 2, 180 00, Prague 8, Czech Republic
[c] Institute for Inorganic Chemistry, Graz University of Technology, Stremayrgasse 9, 8010, Graz, Austria

ARTICLE INFO

Handling Editor: Dr A Iranzo

Keywords:
Catalyst degradation
PEMFC
SAXS
Operando
ORR

ABSTRACT

Detailed multi-technique characterization of catalyst layer degradation is fundamental for improving catalyst stability and performances in Proton Exchange Membrane Fuel Cells (PEMFCs), and Small Angle X-Ray Scattering (SAXS) coupled to chemical and/or electrochemical analysis can provide important insights of processes involved in catalyst coarsening. In this extent, we present an approach to SAXS analysis able to describe all of the layers composing the Membrane Electrode Assembly (MEA): electrolyte, catalyst support, catalyst nanoparticles, and gas diffusion layers. This approach was used to compare morphological evolution of small clusters formed by catalyst nanoparticles in pristine and aged MEAs in both *ex situ* and *in operando* conditions, on a standard SAXS beamline, without exploiting the advantages of anomalous SAXS. Twin MEAs were aged with two different types of Accelerated Stress Tests (AST): one addressed to the catalyst support (s-AST) and one targeting the catalyst layer (c-AST). Limited growth of catalyst nanoparticle size was found when running s-AST, while remarkable evolution was revealed once applying c-AST. Such a difference was mainly reconducted to the disconnection of catalyst nanoparticles from the electrical paths, as supported by analysis of specific Electrochemically Active Surface Area (ECSA). In both cases, the small clusters were found becoming more compact after AST were run.

1. Introduction

With the aim to reduce global warming and pollutant emissions, green-hydrogen-fueled Proton Exchange Membrane Fuel Cells (PEMFC) appear to be the most promising technology for converting chemical energy into electricity within a sustainable energy production chain. Due to their high specific power density and to their versatility, PEMFC can play a key role as sustainable powertrains for stationary systems as well as for several types of vehicles (from transportation to equipment dedicated to light- and heavy-duty operations), and several studies demonstrated their efficiency as stand-alone systems or also in combination with batteries [1–3]. Nonetheless, broad PEMFC diffusion on the market is still limited by high production costs, which is mainly due to the amount of platinum needed to be used as a catalyst material.

PEMFC technology had widely improved during the last decades, in terms of both cost reduction (by reducing the platinum content) and increase of system lifetime. Such technological development was also promoted by the enhanced level of detail offered by *in operando* electrochemical analyses [4] combined with in *operando* investigations with X-Ray- and/or neutron-based investigation techniques, which allowed to shed light onto the main processes ruling catalyst behavior and at the basis of their degradation. While neutrons were mainly exploited for investigations related to water management in PEMFC [5–7], X-Ray--based analyses mainly provided insights about chemical and morphological evolution of the catalyst layer [8–16]. In this framework, Small Angle X-Ray Scattering (SAXS) is the method of choice to study morphological changes occurring at the nanoscale, such as Ostwald ripening or particle detachment. However, the complex (multi-layered) architecture constituting the Membrane Electrode Assembly (MEA) can be an obstacle in developing a reliable model for SAXS data analyses if SAXS is not carried out in anomalous conditions, where the tunable energy of the incoming beam allows to add chemical sensitivity to the technique, and consequently guarantees the possibility to observe the evolution of the catalyst nanoparticles only. Up to now, for SAXS based

* Corresponding author. Department of Engineering and Architecture, University of Trieste, Via A. Valerio 10/1, 34127, Trieste (TS), Italy.
** Corresponding author.
E-mail addresses: marco.bogar@dia.units.it (M. Bogar), yurii.yakovlev@mff.cuni.cz (Y. Yakovlev).

https://doi.org/10.1016/j.ijhydene.2024.01.261
Received 1 June 2023; Received in revised form 13 January 2024; Accepted 21 January 2024
Available online 10 February 2024

studies of MEA for PEMFC different approaches were found: some models were developed focusing the analyses to the electrolytic membrane of the MEA only [12,17], while other approaches were addressed to the catalyst layer, measured in both *ex situ* [16,18,19], *in situ* [20–23], and *in operando* conditions [10,13,14,24].

With this work, we want to adapt the expertise achieved with *in situ* SAXS studies about degradation phenomena occurring at the surface of a model system for the Oxygen Reduction Reaction (ORR) for PEMFCs [25–27] to real MEAs. The model needed to be adapted including all of the components constituting the MEA by means of a layer-by-layer approach. In addition to other SAXS models already developed for studying fuel cell catalyst layers (such as in the work of Martens et al. [14]), we introduced a term describing particle clustering (analogously as made by Povia et al. [10]) by means of a structure factor term (as highlighted in previous works addressing to catalyst layers in fuel cells [10,28], or also to systems composed by a set of supporting and decorating nanoparticles in general [29–31]). In addition, the formulation of the model was developed in the framework provided by the theoretical and experimental studies carried out by Asset, Gommes and co-workers [13,32,33]. The approach was carried out without having the opportunity to exploit the advantage of the chemical sensitivity provided by measuring SAXS in anomalous conditions. Moreover, the proposed approach uses a fully analytical model, providing computational advantages with respect models based on numerical integration. The model was then validated: (i) to quantify the degradation effects induced by applying two different types of Accelerated Stress Tests (AST) of a commercial catalyst layer via *ex situ* SAXS analysis, and (ii) by repeating the previous analysis by means of *in operando* SAXS measurements.

2. Material and methods

2.1. MEA preparation

Fuel cells were assembled using self-made Catalyst Coated Membranes (CCM) sandwiched between two commercial gas diffusion layers (GDLs, H24C5, Freudenberg). CCM were prepared by ultrasonic spraying of the catalyst ink on the surface of an ionomeric membrane (Nafion® NR-211, FuelCellStore) using a CNC controlled system (ExactaCoat, Sono-Tek). Details of the catalyst ink preparation and basic testing are described in our previous works [34,35]. In short, Pt/C catalyst particles (Pt on Vulcan XC-72R, 40 %; FuelCellStore), ionomer dispersion D521 (5 % 1100 EW; FuelCellStore) and isopropanol/acetone solvent (1:1 ratio) were ultrasonically mixed to form catalyst ink. Ink formulation was tuned to keep the ionomer-to-carbon ratio of 0.6. The membrane was secured on a hot-bed (60 °C) during spraying process. Anode catalyst loading of 0.05 $mg_{Pt}\cdot cm^{-2}$ and cathode catalyst loading of 0.8 $mg_{Pt}\cdot cm^{-2}$ were achieved by adjusting number of spraying cycles.

2.2. Electrochemical analysis

MEAs further measured *ex situ*, were clamped in the graphite cell fixture with meander-like flow field design and active area of 4 cm^2. Measurements of fuel cell characteristics were performed at 80 °C and 100 % Relative Humidity (RH). Potentiostats PTC-0520E (Kolibrik.net) and SP-150 (Bio-Logic) were used for measurements of polarization curves and Cyclic Voltammetry (CV), respectively. Polarization curves were recorded in galvanostatic mode, increasing current every 10 s by 5 mA cm^{-2} per step. Cyclic voltammograms were recorded in the range of potentials from 0.05 to 1 V using scan rates of 20, 50 and 100 mV s^{-1}. Potentiostatic Electrochemical Impedance Spectroscopy (PEIS) was performed using the potentiostat SP-150 in the frequency range 1 Hz ÷ 100 kHz at polarization voltage of 0.85 V and with excitation amplitude of 5 mV peak-to-peak.

Two types of Accelerated Stress Tests (AST) were performed. Support-oriented Accelerated Stress Tests (s-AST) were used to accelerate carbon-based support electrochemical corrosion, simulating a cathode voltage surge at fuel cell start-up/shut-down sequence and consisted in applying cyclic voltammetry from 1 to 1.5 V at the sweep rate of 500 mV s^{-1} for 5000 cycles. Catalyst-oriented Accelerated Stress Tests (c-AST) were performed by step-like potential switching from 0.6 to 0.95 V, keeping each voltage constant for 3 s, for a total number of 30000 cycles. Both protocols were performed at 80 °C and 100 % RH. The anode catalyst layer was used as both reference and counter electrode and fed by H_2 flow (50 sccm). The cathode catalyst layer was configured as a working electrode fed by N_2 flow (50 sccm). ASTs were interrupted in order to record CV for estimation of specific electrochemically active surface area.

The two twin MEAs analysed via *in operando* SAXS were inserted into a properly designed, titanium made, electrochemical cell, provided by a heating system and transmission windows for directly probing the MEA. The cell was designed with an active area of 4 cm^2. A sketch of the experimental setup is represented in Fig. S1. The MEAs were measured in pristine conditions at first. Then, a conditioning protocol (cell temperature: 80 °C, H_2 flown at the anode at 50 sccm and RH: 100 %, N_2 flown at the cathode 50 sccm and RH: 100 %), was used to humidify the MEA and heating the cell. Afterwards, a break-in procedure (cell temperature: 80 °C, H_2 flown at the anode at 50 sccm and RH: 100 %, O_2 flown at the cathode 50 sccm and RH: 100 %, applied potential: 0.4 V) was applied, in order to check the effective fuel cell operation (in Fig. S2 the profile of the current recording during this step is shown). Finally, s-AST and c-AST were respectively run, as previously described. CV curves and impedance spectra were recorded every 250 cycles. While the s-AST could be fully recorded (5000 CV), due to beamtime limitations the c-AST could be recorded up to (4000 CV).

2.3. Electron microscopy

Scanning Electron Microscopy (SEM) images were collected from samples measured *ex situ* using a Tescan MIRA III microscope operating at 30 keV electron beam energy. Transmission Electron Microscopy (TEM) micrographs were measured using a JEOL JEM NEOARM-200F operated at 200 kV. Samples were prepared rubbing a catalyst layer against a copper holey carbon TEM grid. Particle size distribution was calculated by means of ImageJ software by manually measuring the area of catalyst particles on calibrated images. For every image were analysed at least 100 particles. Particle diameter (D) was calculated from the measured area (A) as $D = 2\sqrt{A/\pi}$.

2.4. Small angle X-ray scattering

SAXS measurements were conducted in transmission mode. Samples analysed *ex situ*, were measured at room temperature and pressure on the Austrian SAXS beamline at the ELETTRA synchrotron in Trieste, Italy [36], at the wavelength of 1.54 Å (8 keV). Scattering patterns were recorded by means of a 2D pixel detector (Pilatus 3 1 M, Dectris) at a sample-to-detector distance of 1746.50 mm, providing a q-range from 0.054 nm^{-1} to 4.131 nm^{-1}. Samples measured *in operando* conditions were measured at the same beamline at room temperature and pressure with a beam energy of 0.77 Å (16 keV) by means of a home-made electrochemical cell. Sample-to-detector distance was set to 2225.707 mm, providing a q-range from 0.098 nm^{-1} to 6.413 nm^{-1}. In both setups, silver behenate were used as calibrants. Catalyst powder and catalyst ink were measured with a laboratory SAXS instrument (SAXSpoint 2.0, from Institute of Inorganic Chemistry at the Graz University of Technology), supplied with a 2D pixel detector (EIGER2 R 1 M, Dectris). The software SAXSDOG [37] was used to integrate radially the recorded patterns into mono-dimensional patterns ($I(q) \pm \delta I$), while IGOR Pro software (IGOR Pro 7.0.8.1, Wavemetrics) was used for normalization by transmission values, background subtraction and fitting.

2.5. SAXS modelling, results and discussion

MEAs are composed by a CCM sandwiched in between two Gas Diffusion Layers (GDL). Historically, the modelling of the CCM for SAXS analysis evolved during the years, and more recently the leading approach is represented by modelling the substrate nanoparticles and the decorating catalyst nanoparticles as two set of spheres of different size. In addition to the two scattering contributions due to these two particle populations, this approach includes the so-called cross-correlation term, resulting from the mutual position among support and decorating particles [29]. The introduction of this term for the modelling of catalyst nanoparticles deposited on a microporous substrate was theorized by Gommes et al. [32], and its existence was experimentally reported by both Asset and co-workers [13] and by Tiller et al. [38] by using standard and anomalous SAXS, respectively. More in depth, Gommes and co-workers [33] also provided a formulation of a series of approximations of their initial formulation, highlighting as the cross-correlation term may not be dominant for specific architectures and catalyst loadings. More in depth, they show as under low catalyst loadings, the contribution from the cross-correlation is much smaller than the contribution for the support itself, and in such conditions, the scattering contributions of support and catalyst nanoparticles can be added incoherently [33]. In a dedicated section in Supplementary Information we discuss the effective detectability of the cross-correlation term for the MEAs characterized in this work, concluding that its contribution can be considered negligible when moving from the analysis of CCMs to MEAs. That is, in order to build up an analytical model for fitting the SAXS patterns, all of the contributions can be incoherently added:

$$I_{MEA}(q) = B + I_N(q) + I_V(q) + I_C(q) + I_G(q) \quad (1)$$

where B represents the constant background, and the four terms $I_X(q)$ model the different components of the MEA: (N) the Nafion membrane, (V) the Vulcan substrate hosting the catalyst nanoparticles, (C) the catalyst nanoparticles and (G) the GDL. Because this work is focused to investigate the effects of AST on the catalyst layer, the expression can be simplified as:

$$I_{MEA}(q) = B + I_S(q) + I_C(q) \quad (2)$$

where all of the components not describing the Pt nanoparticles are grouped within the term $I_S(q)$. Model building up started form the analysis of the electrolytic membrane (Nafion® NR-211). As extensively reported in literature [39], Nafion scattering pattern is characterized by two peaks and an upturn in the low-q region. In particular, and at room conditions, the so-called Ionomer Peak (IP, generated from the spatial arrangement of the ionomeric-hydrophilic regions) is found around 2 nm^{-1} while the so-called matrix knee (MK, due to the clustering of the polymeric-hydrophobic backbones) can be observed around 0.6 nm^{-1}. Such features have been often modelled by means of Gaussian functions, in order to determine peak position and width. Nonetheless, we compared data fitting carried out by using three different probability distribution functions: Gaussian, Lorentzian and Voigt [40–44] ones (more details about Nafion modelling are provided in Supplementary Information). To all of them, a power law was added for describing the intensity upturn in the low-q region.

From fit results, it was found as the best model for data fitting was the one based on the Voigt peaks, providing the lowest value of reduced χ^2 (Fig. 1 and Table S1). Afterwards, the bilayer composed by the Nafion membrane and the Vulcan substrate was measured (Fig. 2a). Vulcan is constituted by large spherical-like particles arranged in a porous structure. According to the results obtained from preliminary characterization of the catalyst ink, showing as the power law used to model the Nafion/Vulcan dispersion has an exponent close to the value of four (more details about in Supplementary Information), this layer was modelled by using the form factor developed by Debye, Anderson and Brumberger (DAB) [45,46], with the aim of relating the average size of carbon supports hosting the catalyst nanoparticles to the correlation length parameter of the model. The DAB form factor was thus added to the two Voigt peaks describing the Nafion membrane:

$$I_S(q) = B + \alpha \cdot \left[\frac{C_N}{q^{p_N}} + I_{IP} \cdot V(w_{IP} \cdot (q - q_{IP}), s_{IP}) + I_{MK} \cdot V(w_{MK} \cdot (q - q_{MK}), s_{MK}) \right] + \frac{A}{\left(1 + (q \cdot \xi_V)^2\right)^2} \quad (3)$$

where B defines the background, A defines the forwarded scattering probability of the DAB model and ξ_V is the correlation length parameter which is related to the minimum size of the Vulcan features. The function V represents the Voigt peak function of both peaks, ionomer and matrix knee (x = IP, MK) having intensity I_X, width w_X, position q_X, and shape factor s_X (defining the balance between Gaussian and Lorentzian contributions). By assuming that there are no changes in Nafion morphology once the Vulcan layer is added, when fitting the bilayer composed by Nafion and Vulcan substrates, the parameters previously obtained by fitting the bare Nafion were kept fixed, and only the α parameter was let free, in order to highlight any variation in scattering intensity with respect to the analysis of the bare Nafion membrane. Fit results are show in Fig. 2a, together with the contribution of the single components from the model. From a quantitative point of view, the correctness of the result is deducted from the values of the scaling factor α (equal to 1.02 ± 0.01), meaning that Nafion scattering patterns is not varying when the ionomer is sandwiched in between two Vulcan layers, as expectable. The value of the exponent of the power law term (p_N, equal to 1.97 ± 0.01), was found consistent with the scattering

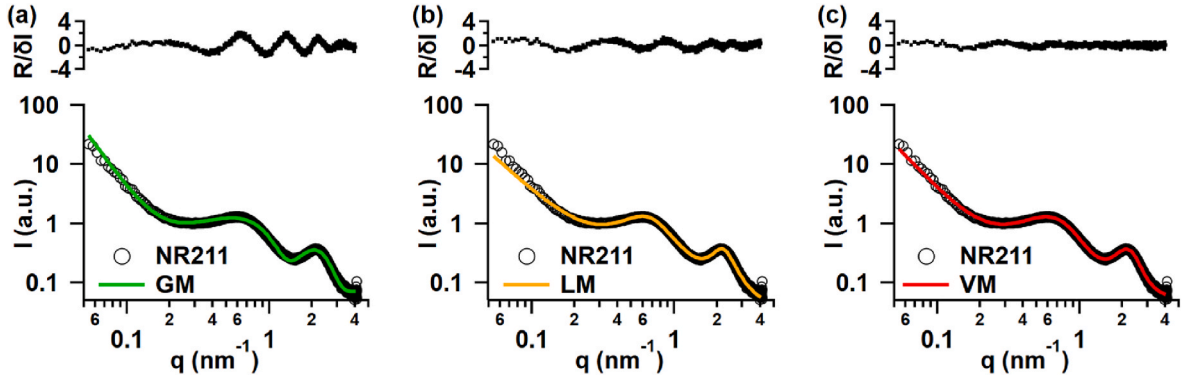

Fig. 1. Nafion SAXS modelling. Comparison among fitting results of the Nafion scattering pattern by using a power law together with: (a) two Gaussian peaks (GM), (b) two Lorentzian peaks (LM) and (c) two Voigt peaks (VM). Normalized fit residuals (fit residuals, R, weighted by the error, δI) are appended on top of each graph, while complete results are listed in Table S1.

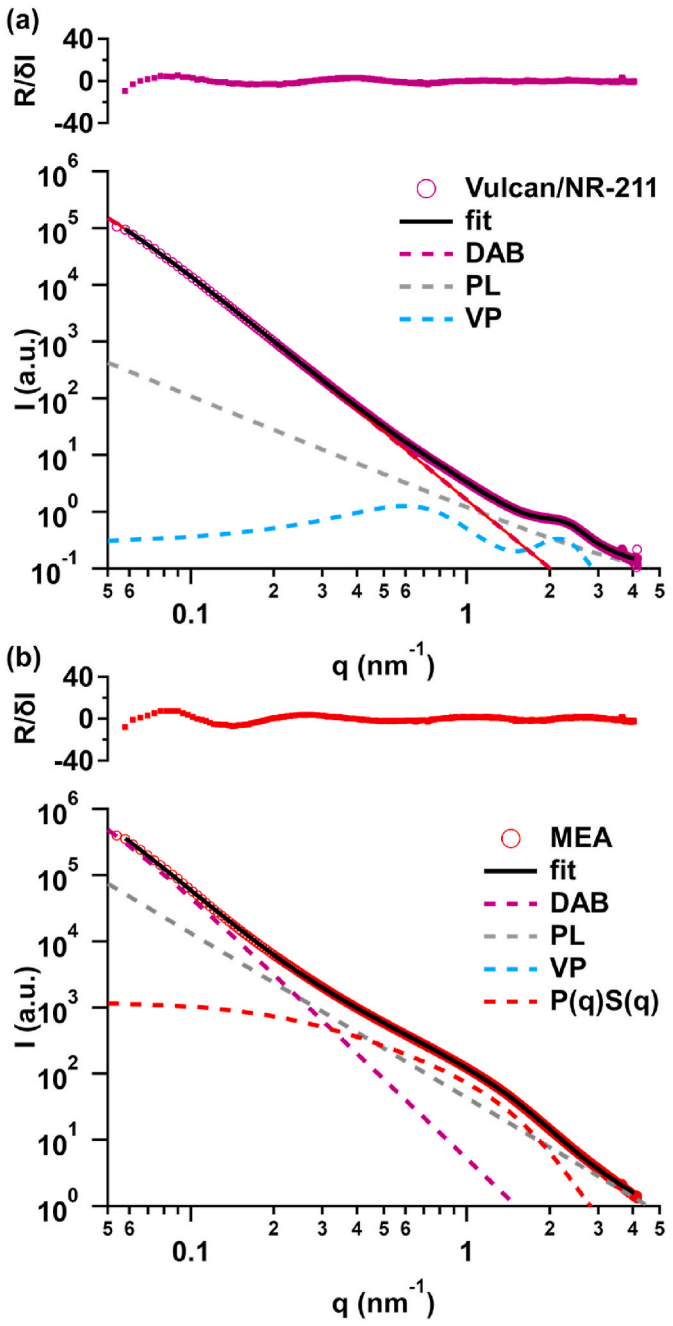

Fig. 2. SAXS modelling the full MEA. SAXS patterns of (a) the Vulcan/Nafion NR-211 bilayer, and (b) the full MEA, recorded in pristine conditions. In both graphs the deconvoluted components of the fitting model, are also shown: the two Voigt peaks used for modelling Nafion (VP), the power law (PL) and the Debye-Anderson-Brumberger model (DAB) used for representing the Vulcan support. Catalyst nanoparticles are finally represented by means of the product of the form factor P(q) and the structure factor S(q); the contribution from bare form factor, P(q), is also shown. Normalized fit residuals (fit residuals, R, weighted by the error, δI) are appended on top of each graph.

produced by clustered-networked mass fractal structures, in agreement with previous analysis carried out on Nafion [47–49]. The minimum size of Vulcan aggregates, $\overline{D_V}$, was retrieved from value of ξ_V (equal to 36.07 ± 0.08 nm), by comparing the Taylor expansions of the DAB model and the Guinier approximation for spherical particles [50], resulting in: $\overline{D_V} = \sqrt{10}\,\xi_V$. Consequently it turns out as $\overline{D_V} = 114.06 \pm 0.25$ nm, in agreement with micrographs collected on previous analysis [34], and with SEM images collected from the pristine sample (Fig. S3a), where Vulcan agglomerates of around 100 nm are revealed.

Then, the full MEA, composed by electrolyte, catalyst support, catalyst nanoparticles, and GDL, was measured. In Supplementary Information, the effective detectability of the cross-correlation term among catalyst and support nanoparticles is properly discussed. There, it is also claimed as, in the framework of *in operando* analysis of full MEAs, the incoherent sum of the terms describing the support and the decorating nanoparticles can be considered acceptable. The major advantage in that, is related the opportunity to adopt analytical models for the size distribution, which would strongly simplify the analysis from a computational point of view. Thus, the catalyst nanoparticle population is described by a product of a form factor P(q) and a structure factor S(q):

$$I_{MEA}(q) = B + P_{Naf} + \frac{A}{\left(1 + (q\cdot\xi_V)^2\right)^2} + I_P\cdot P(D_P, \sigma_P, q)\cdot S\left(\xi, D_f, q\right) + \frac{C}{q^p} \quad (4)$$

Here the term

$$P_{Naf} = \alpha\cdot[I_{IP}\cdot V(w_{IP}\cdot(q - q_{IP}), s_{IP}) + I_{MK}\cdot V(w_{MK}\cdot(q - q_{MK}), s_{MK})]$$

represents the Nafion membrane (the upturn of Nafion, previously described by means of the term C_N/q^{p_N} was neglected because no more detectable). As a form factor, a set of polydispersed spheres following the Schulz distribution was used: here, I_P represents the forwarded scattering probability of catalyst nanoparticles, D_P their mean particle diameter, while σ_P the standard deviation from the mean particle diameter, which is directly proportional to particle polydispersity [51, 52]. The main advantage of using the Schultz distribution as a form factor, relies in the fact that, being a fully analytical model, numerical integration is not required, and the fitting procedure is computed in shorter times. Moreover, as it is known that Ostwald ripening (one of the predominant phenomena involved in catalyst degradation) was observed modifying the particle size distribution shape far from the log-normal profile [53], the Schultz distribution becomes a valuable alternative for describing particle coarsening. In the formulation of the cross-correlation terms within the so-called 'raspberry' model [29], the leading term describing the population of particles deposited at the surface of a supporting one, is represented by product of a particle form factor by a sin(x)/x interference term (Debye equation [49]). In this work, since catalyst nanoparticles are aggregated into clusters (as depicted in Figs. S3 and S4), their state of agglomeration was chosen to be described by means of the model proposed by Teixeira [47] to investigate fractal systems, as already done by Povia and co-workers [10]: here D_f is the fractal dimension, a parameter related to the morphology of the clyster shape, while ξ is the cut-off distance describing the behavior of the pair correlation function for larger distances than the size of a catalyst nanoparticle. As described by Teixeira [47], ξ is a qualitative marker and it represents the cut-off distance above which the mass distribution of the sample is no longer described by the fractal law. Thus, it can be used to represent the correlation length in a disordered material or the average cluster size [47]. Being the MEA loaded with nanoparticles arranged in small clusters, the cut-off distance was chosen as a marker of the average cluster size. From ξ, the value of the corresponding radius of gyration, R_g, can be retrieved by means of: $R_g^2 = \xi^2\cdot[D_f\cdot(D_f + 1)]/2$ [54]. The model here developed was built with the aim of investigating catalyst nanoparticle evolution at the cathode side of a PEMFC, thus, the presence of catalyst nanoparticles at the anode side must be considered. To avoid the superimposition of the scattering footprints due to the particle populations deposited at the two electrodes, a strongly asymmetrical catalyst loading was used (anode: 0.05 mg_{Pt}/cm^2, cathode: 0.8 mg_{Pt}/cm^2). In fact: (i) being the cathode loading 16 times bigger than anode one, knowing that (ii) scattering forwarded probability scales with the particle volume (that is the third power of the radius), aware that (iii) the gas diffusion layers introduce a strong background (from which the signal-to-noise of the scattering

pattern due to the catalyst nanoparticles gets lower, Fig. S5), and assuming that (iv) anode particles were not undergoing to any remarkable evolution during fuel cell operation (due to the fact that the anode potential is close to zero), the contribution from the anode particle population can be considered being negligible. Fit results are shown in Fig. 2b, together with the deconvolution components of the MEA: here, the scattering contribution due to Nafion (overall in the q-range in which the matrix knee is found) is at least two orders of magnitude less intense than the component used to model the catalyst nanoparticles, and it can be considered negligible. By repeating the fit including and excluding the Nafion contribution (Fig. S6 and Table S2) it turns out as the term describing the Nafion membrane can be excluded from the model. Nonetheless, this assumption holds at room conditions only: from previous analyses conducted on Nafion [7,55–58], it is clear as, at higher hydration rates of the membrane (such as a fully humidified MEA working in a PEMFC), also its forwarded scattering contribution rises in magnitude and a more accurate approach needs to be used for *in situ* and *in operando* analyses (as it will be later shown). From fitting the scattering pattern collected from the pristine MEA, the mean particle diameter was found equal to 2.20 ± 0.01 nm, in agreement with the technical specifications provided from the manufacturer [59]. From the parameters composing the structure factor, it turns out that particle are aggregated forming clusters resembling branched/mono-dimensional -like, mass fractal aggregates ($D_f \cong 1.6$) [47] having a cut-off distance of about 8.05 ± 0.23 nm, corresponding on an average fractal size (R_g) of 8.29 ± 0.07 nm. Obtained results were found in agreement with microscopy images. In fact, from TEM micrographs quasi-linear arrangements (or branched-like ones) can be detected (Fig. S4). Fit results were also found in agreement with the preliminary characterization of the catalyst powder and the catalyst ink, as detailed in the dedicated chapter provided in Supplementary Information (and in Fig. S7 and Table S3).

The so-developed model was then used to characterize catalyst degradation of two twin MEAs undergone two different types of AST, as summarized in Fig. 3. Here polarization curves and impedance spectra at the beginning and at the end of tests are compared (BOT and EOT, respectively). As expected, polarization curves highlight reduction of fuel cell performances in both of the cases (Fig. 3a and b). However, it is difficult to get clear understanding of the underlying processes from polarization curves only, due to the plethora of different factors influencing the final performance. To get more detailed understanding about changes induced in catalyst layers, Electrochemical Impedance Spectroscopy (EIS) was recorded at the beginning of tests, at an intermediate state (at the 2000th cycle for s-AST, at the 10000th cycle for c-AST), and at the end of tests; results are displayed in Fig. 3c and d. All of the measured spectra are characterized by one dominating semi-circle, which is originating from the cathode catalyst layer (the anode semicircle is virtually undetectable), and for both protocols no changes can be revealed involving the high frequency resistance (leftmost intercept with real impedance), indicating stable ohmic resistance of the fuel cell. Moreover, the measured value of ~50 mOhm·cm^2 is close to one reported for similar systems [60]. However, the diameter of the semicircle increases during the stress protocols, corresponding to increase of the charge transfer resistance and, therefore, to induced degradation of the catalyst material, in agreement with the recorded reduction in catalyst performances. Such changes can be caused by the evolution of catalyst particles morphology, which can be corroborated by measurements of specific Electrochemically active Surface Area (ECSA), which can be calculated by comparing the evolution of active area of catalyst during stress test protocols as [61]:

$$ECSA = \frac{Q(H_{UPD})}{C \cdot m_{Pt}} \tag{5}$$

Where $Q(H_{UPD})$ is the underpotential deposited hydrogen charge (obtained by integrating the current values within the hydrogen desorption region), C is the hydrogen adsorption charge on a smooth Pt electrode (equal to 210 μC·cm^{-2}), and m_{Pt} is the mass of the catalyst loading per unit area. From cyclic voltammograms recorded while running AST (Fig. S8) ECSA evolution was retrieved (Fig. 3e and f): while AST were running, progressive decrease in the ECSA is observed. This can be caused by various reasons, as enlargement of catalyst particles, their detachment from support, and/or a combination of both. Post-mortem *ex situ* SAXS was thus used to complement electrochemical results. Recorded scattering patters are compared in Fig. 4a and 4c together with calculated particle size distribution, obtained by fitting the scattering patterns by means of the model previously discussed, while a complete

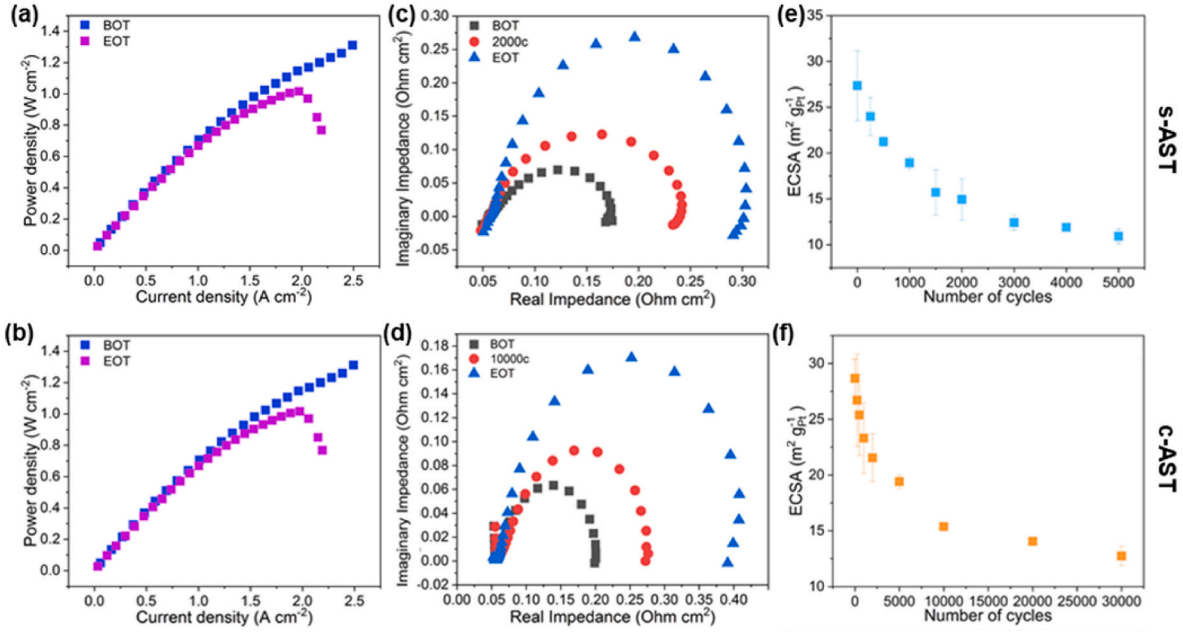

Fig. 3. Electrochemical characterization. (left) Fuel cell power density curves measured before (Beginning of Test, BOT) and after (End of Test, EOT) running (a) support- and (b) catalyst-oriented AST (s-AST and c-AST, respectively). (center) Nyquist plots evolution during (c) s-AST and (d) c-AST. (right) Evolution of specific Electrochemically active Surface Area (ECSA) during (e) s-AST and (f) c-AST.

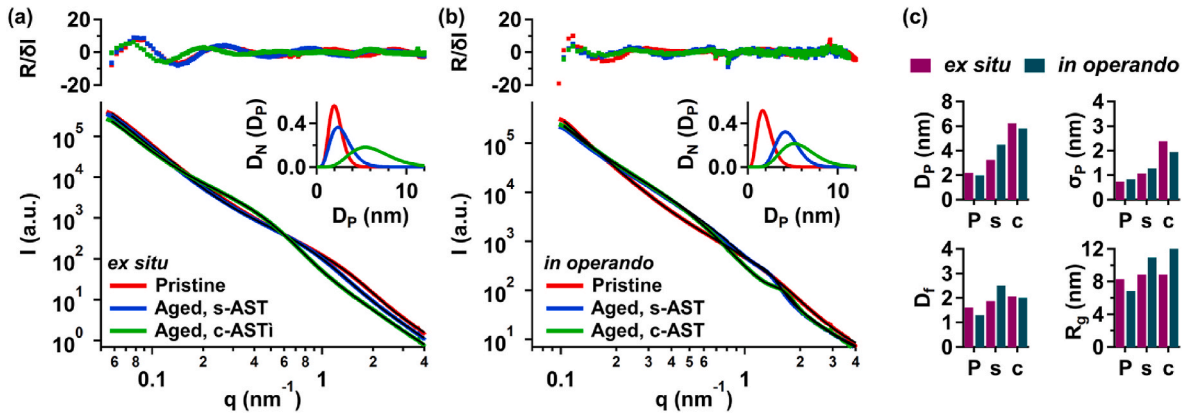

Fig. 4. Model validation in *ex situ* and *in operando* measurements. Comparison of SAXS patterns recorded from pristine MEA, MEA undergone s-AST, and MEA undergone c-AST in (a) *ex situ* and (b) *in operando* conditions. Particle size distribution evolution, calculated from fit results is shown as an insert in each graph. Normalized fit residuals (fit residuals, R, weighted by the error, δI) are appended on top of each graph. (c) Comparison of the variation of the main parameters form the proposed model after fitting the patterns represented in Fig. 4a and b mean particle diameter (D_P) and standard deviation from the mean diameter (σ_P) within the Schultz distribution, fractal dimension (D_f), and cut-off distance (ξ). P: pristine, s: after s-AST, c: after c-AST.

overlook on fit results is provided in Table S4. TEM (Figs. S4b and S4c) were used to complete the post-mortem characterization.

When studying the aged samples, it was found as after having run the s-AST, the nature of particle cluster changed, moving towards a more compact mass fractal (fractal dimension value is changing from 1.62 to 1.88). In addition, also particle size and polydispersity were found to slightly increase, as well as average cluster size, as represented in Fig. 4c and listed in Table S4. Due to the fact that the s-AST is developing over the potentials which are inducing carbon corrosion, such a limited evolution of variation in particle size is supposed to be related to enhanced particle detachment from the support and/or to particle unlinking from the electronic conduction paths. On contrary, the evolution of particle size distribution after having run c-AST highlighted that catalyst degradation mainly reflects in an increase of mean particle diameter (to 6.24 ± 0.02 nm) and polydispersity (Fig. 4a and c). Moreover, the shape of the retrieved particle size distribution at the end of AST, is less skewed towards lower particle size values, suggesting that Ostwald ripening is the main cause leading to the increase of particle size, as previously observed [24,27,62]. With respect to pristine conditions, it was also found as fractal dimension grows up to 2.07, indicating the formation of a compact mass fractals, which size is almost coincident with mean particle size ($R_g = 8.86 \pm 0.15$ nm), as detailed Fig. 4c in and in Table S4. This result is also in agreement with post-mortem TEM (Fig. S4b), where more compact, bigger, and stand-alone particles can be observed.

In trying to connect electrochemical results with morphological analysis, a quantitative comparison was made by means of a simple geometrical model, which was used to relate the changes revealed in ECSA to the variation of particle size distribution recorded by SAXS: here, the ratio among ECSA at the beginning (subscript *i*) and at the end (*f*) of AST was calculated within two assumptions: (i) the leakage of catalyst material from the electrode during the AST is negligible, that is, that the probed Pt mass in the catalyst layer remains constant (within this assumption particle detachment is meant to mostly induce disconnection of catalyst nanoparticles from the electric conduction paths), and (ii) once c-AST are applied, the decrease of active area of particles is caused solely by catalyst dissolution and redeposition rather than by detachment from their support, as expected by the lower than 1.0 V upper potential reached by the stress test. Within these assumptions, the ratio among specific ECSA values (ζ_{EC}), can be expressed as:

$$\zeta_{EC} = \frac{ECSA_i}{ECSA_f} \tag{6}$$

Such a ratio needs to be compared to the ratio (ζ_{SX}) of the specific catalyst surface areas (SA) calculated at the same time points from parameters related to the particle size distribution:

$$\zeta_{SX} = \frac{SA_i}{SA_f} \tag{7}$$

Here, the specific surface area is calculated as previously done by Povia and co-workers [10], as:

$$SA = \frac{6\langle D^2\rangle}{\rho\langle D^3\rangle} = \frac{\langle \mathrm{A}\rangle}{\rho\langle \mathrm{V}\rangle} \tag{8}$$

where ⟨A⟩ and ⟨V⟩ are respectively the average surface area and the average volume of the probed catalyst nanoparticles, respectively calculated as the second and the third moment of the Schulz probability distribution function, $f(r)$ [63,64]:

$$\langle A\rangle = 4\pi \int_0^\infty f(\mathrm{r})\mathrm{r}^2 dr \tag{9}$$

$$\langle \mathrm{V}\rangle = \frac{4}{3}\pi \int_0^\infty f(\mathrm{r})\mathrm{r}^3 dr \tag{10}$$

Table 1
Comparing electrochemical and *ex situ* SAXS results. Comparison of main results obtained from electrochemical analysis and SAXS data fitting retrieved from MEAs in pristine conditions, after aging with s-AST (5000 CV cycles), and after aging with c-AST (30000 CV cycles). From SAXS analysis, values of mean particle diameter (D_P) are listed together with calculated average particle surface area (⟨A⟩) and volume (⟨V⟩), calculated within the Schulz distribution. From electrochemical analysis, specific electrochemically active surface area (ECSA) is listed, calculated by averaging three measurements. Finally, the surface growth rate calculated from both electrochemical measurements (ζ_{EC}) and from SAXS analysis (ζ_{SX}) are shown.

	D_P, nm	⟨A⟩, nm^2	⟨V⟩, nm^3	ECSA, m^2/g$_{Pt}$	ζ_{EC}	ζ_{SX}
Pristine	2.20 ± 0.01	4.71	7.69	27.3 ± 3.8	–	–
After s-AST	3.28 ± 0.01	8.03	17.12	10.9 ± 0.8	2.51 ± 0.53	1.31
After c-AST	6.24 ± 0.02	30.57	127.15	12.7 ± 0.8	2.14 ± 0.45	2.55

Table 2
Comparing electrochemical and *in operando* SAXS results. Comparison of main results obtained from electrochemical analysis and SAXS data fitting retrieved from MEAs in pristine conditions, after aging with s-AST (5000 CV cycles), and after aging with c-AST (4000 CV cycles). From SAXS analyses, values of mean particle diameter (D_P) are listed together with calculated average particle surface area (⟨A⟩) and volume (⟨V⟩), calculated within the Schulz distribution. From electrochemical analysis, specific electrochemically active surface area (ECSA) is listed. Finally, the surface growth rate calculated from both electrochemical measurements (ζ_{EC}) and from SAXS analysis (ζ_{SX}) are shown.

	D_P, nm	$\langle A \rangle$, nm^2	$\langle V \rangle$, nm^3	ECSA, m^2/g$_{Pt}$	ζ_{EC}	ζ_{SX}
Pristine	1.99 ± 0.04	3.10	4.10	28.6	–	–
After s-AST	4.51 ± 0.01	15.98	48.03	9.4	3.05	2.27
After c-AST	5.81 ± 0.07	26.54	102.82	10.9	2.56	2.93

Results are listed in Table 1: at a first glimpse, a slight discrepancy between results is recorded when c-AST are performed. In fact, while ζ_{EC} is equal to 2.14 ± 0.45, ζ_{SX} is equal to 2.55. Such discrepancy can be easily explained by some uncertainties in the measurements, to the reduced sensitivity of SAXS to the smallest particles present on the MEA (which are strongly contributing to the specific electrochemically active surface area), as well as to the fact that the ECSA of a single nanoparticle is not equivalent to a spherical surface, due to the fact that a part of the particle is in contact with the Vulcan support. On the other hand, the discrepancy observed for the s-AST, is much larger: in these conditions ζ_{SX} is equal to 1.31 whereas ζ_{EC} was found corresponding to 2.51 ± 0.53. This fact evidences the presence of additional mechanism causing ECSA losses: since in s-AST Pt/Vulcan catalyst is subjected to higher potentials (with respect c-AST), carbon corrosion leads to catalyst detachment and/or unlinking from the electronic conduction paths. Therefore, once detached (or disconnected), catalyst particles are neither subjected to size changes during the stress protocol nor contributing to total electrochemical area. Being this a dynamical process, it is not possible to get further insights into size distribution of attached and detached particles.

Finally, the model was validated also during *in operando* analysis carried out on a couple of pristine MEAs undergone to s-AST and c-AST (Fig. 4b). While *operando* analysis could be fully repeated for the MEA undergoing s-AST, time limitations constrained the analysis of the MEA aged via c-AST to 4000 CV cycles. However, as demonstrated in other studies, degradation is considered to be more consistent during the first few thousand of cycles [14], and the reached time point can be assumed being comparable to the *ex situ* sample (where the c-AST was run completely). By comparing the scattering patterns recorded *ex situ* and *in operando* is evident as aged patterns differ remarkably in the high-q region. Such a difference can be related to the operative conditions of the fuel cell, where the MEA was operated at 100 % RH and the Nafion membrane was fully hydrated. The level of Nafion hydration reflects on its scattering pattern as a shift towards lower q values and an increase of the intensity of the ionomer peak (in Fig. 4b can be spotted around 1.4 nm^{-1}), while the matrix knee morphology does not vary considerably (mostly rising in intensity) [55–58]. The effects on Nafion hydration and the comparison with the scattering patterns collected from the MEAs (represented in Fig. 4b) are better displayed in Fig. S9, where the Nafion scattering patterns were recorded in pristine conditions and after having run the same conditioning protocol used for the MEAs inside the same electrochemical cell. By fitting the scattering patterns collected *in operando* with the model presented in Eq. (4) (with α = 1, and by letting free the intensity parameters of the Voigt peaks), no clear presence of the matrix knee was revealed. Consequently, it was assumed that the scattering contribution of the matrix knee can be neglected, and that *in operando* conditions, the model used for fitting the scattering patterns can be composed by one Voigt peak only for describing the presence of the ionomer peak:

$$I_{MEA}(q) = B + I_{IP}\cdot V(w_{IP}\cdot(q - q_{IP}), s_{IP}) + \frac{A}{\left(1 + (q\cdot\xi_V)^2\right)^2} + I_P\cdot P(D_P, \sigma_P, q)\cdot S(\xi, D_f, q) + \frac{C}{q^p} \quad (11)$$

Fit results are summarized in Table S5, while Fig. S10 shows the deconvoluted components of the model, for each pattern of Fig. 4a and b, underlying as the changes around 1 nm^{-1} can be linked to the hydration state of the Nafion membrane. Variations of the ionomer peak position, were found in agreement with EIS analysis, from where the values of electrical resistance of the MEA, R_0, where extracted: a lower membrane resistance value was recorded when the ionomer peak was found shifted towards lower q-values (Table S6), indicating a higher level of hydration of the Nafion membrane. Finally, SAXS results were related to the electrochemical ones, as summarized in Table 2. Again, lager particle growth was found while running c-AST with respect s-AST, in agreement with previous observations. As expected, once running c-AST most of the whole degradation is taking place during the early stages of catalyst stressing [14,27], while more pronounced growth was found characterizing the particle population during s-AST. Although such a discrepancy in results can be partially related to the noisier environment in which *in operando* measurements are carried out, it could be also related to a more variable operation regime of the cell, but a detailed comparison of these two environmental conditions exceeds the aim of this paper, and will be at the base for a further study, centred on time-resolved *in operando* analyses.

3. Conclusions

To conclude, an effective approach to be used for studying catalyst degradation by means of SAXS analysis was here presented. The model developed for this study was built adopting a layer-by-layer approach, thus by describing all of the layers composing the MEA. Voigt peaks were found to better represent the ionomer peak and the matrix knee representative of the electrolytic membrane, the DAB model was used to model the Vulcan substrate, a set of spheres following the Schulz distribution and clustering into mass fractals was used to characterize the catalyst layer formed by Pt nanoparticles, and a power law was used to represent the bigger features composing the GDL. Then, it was shown as this model (and SAXS characterization more in general) can be used to couple electrochemical measurements in both *ex situ* and *in operando* analyses, providing information about particle size distribution evolution and particle cluster size growth induced by two different types of AST, by means of a simple geometrical model connecting ECSA with SAXS specific surface area. The observed loss of fuel cell performances related to the reduction of ECSA (and highlighted as a reduction of fuel cell performances at the end of both types of AST), could be addressed to different phenomena which were found to differently modify the evolution rates of particle size distribution and cluster size. On both cases, it was observed as catalyst nanoparticles, tending to initially arrange to form branched/mono-dimensional-like clusters, are forming more compact mass fractals during coarsening. Moreover, while running s-AST, support degradation was related to particles disconnection from the electrical paths, thus freezing their growth in size and in cluster growth promoted by particle detachment as well. On contrary, when running c-AST, the reduction of ECSA was linked to Pt dissolution and redeposition causing thus a more pronounced evolution of particle size distribution. Trends revealed with *ex situ* analysis were observed also during *in operando* analysis which are going to be in depth discussed in a future work.

Declaration of competing interest

The authors declare that they have no known competing financial interests or personal relationships that could have appeared to influence the work reported in this paper.

Acknowledgements

All of the authors acknowledge the CERIC-ERIC Consortium for the access to experimental facilities and the financial support. The work was financially supported the Czech Science Foundation, project No. 22-03643S. Y. Y., J. N., A. M. D., and I. M. acknowledge the structural fund project PaC-NG No. CZ.02.1.01/0.0/0.0/16_025/0007414 and financial support and are grateful for the partial financial support provided by the Czech Ministry of Education, Youth and Sports (project LM2018116). M.B. and R.T. acknowledge the financial support from the project sHYpS (sustainable HYdrogen powered Shipping, Horizon Europe call Horizon-CL5-2021-D5-01) and the Italian Operative Program for Research and Innovation 2014–2020 provided by the Italian Ministry of University and Research.

Appendix A. Supplementary data

Supplementary data to this article can be found online at https://doi.org/10.1016/j.ijhydene.2024.01.261.

References

[1] van Biert L, Godjevac M, Visser K, Aravind PV. A review of fuel cell systems for maritime applications. J Power Sources 2016;327:345–64.
[2] Cullen DA, et al. New roads and challenges for fuel cells in heavy-duty transportation. Nat Energy 2021;6:462–74.
[3] Yue M, et al. Hydrogen energy systems: a critical review of technologies, applications, trends and challenges. Renew Sustain Energy Rev 2021;146:111180.
[4] Rabissi C, Zago M, Grahl-Madsen L, Odgaard M, Casalegno A. Local durability optimization of a large-scale direct methanol fuel cell: catalyst layer tuning for homogeneous operation and in-operando detection of localized hydrogen evolution. J Power Sources 2021;506.
[5] Lee J, et al. Neutron imaging of operando proton exchange membrane fuel cell with novel membrane. J Power Sources 2021;496.
[6] Deabate S, Gebel G, Huguet P, Morin A, Pourcelly G. 3 in situ and operando determination of the water content distribution in proton conducting membranes for fuel cells: a critical review. Energy Environ Sci 2012;5:8824–47.
[7] Morin A, et al. Quantitative multi-scale operando diagnosis of water localization inside a fuel cell. J Electrochem Soc 2017;164:F9–21.
[8] Ishiguro N, et al. Operando time-resolved X-ray absorption fine structure study for surface events on a Pt 3 Co/C cathode catalyst in a polymer electrolyte fuel cell during voltage-operating processes. ACS Catal 2012;2:1319–30.
[9] Ishiguro N, et al. Rate enhancements in structural transformations of Pt-Co and Pt-Ni bimetallic cathode catalysts in polymer electrolyte fuel cells studied by in situ time-resolved X-ray absorption fine structure. J Phys Chem C 2014;118:15874–83.
[10] Povia M, et al. Combining SAXS and XAS to study the operando degradation of carbon-supported Pt-nanoparticle fuel cell catalysts. ACS Catal 2018;8:7000–15.
[11] Petkov V, et al. Nanoalloy catalysts inside fuel cells: an atomic-level perspective on the functionality by combined in operando x-ray spectroscopy and total scattering. Nano Energy 2018;49:209–20.
[12] Martinez N, et al. Combined operando high resolution SANS and neutron imaging reveals in-situ local water distribution in an operating fuel cell. ACS Appl Energy Mater 2019;2:8425–33.
[13] Asset T, et al. Disentangling the degradation pathways of highly defective PtNi/C nanostructures - an operando wide and small angle X-ray scattering study. ACS Catal 2019;9:160–7.
[14] Martens I, Chattot R, Drnec J. Decoupling catalyst aggregation, ripening, and coalescence processes inside operating fuel cells. J Power Sources 2022;521:230851.
[15] Chinese T, Ustolin F, Marmiroli B, Amenitsch H, Taccani R. Experimental analysis on the influence of operating profiles on high temperature polymer electrolyte membrane fuel cells. Energies 2021;14:1–14.
[16] Valle F, Zuliani N, Marmiroli B, Amenitsch H, Taccani R. SAXS analysis of catalyst degradation in high temperature PEM fuel cells subjected to accelerated ageing tests. Fuel Cell 2014;14:938–44.
[17] Maccarini M, et al. Submicrometer 3D structural evidence of fuel cell membrane heterogeneous degradation. ACS Macro Lett 2014;3:778–83.
[18] Padgett E, et al. Mitigation of PEM fuel cell catalyst degradation with porous carbon supports. J Electrochem Soc 2019;166:F198–207.
[19] Sievers GW, et al. Self-supported Pt–CoO networks combining high specific activity with high surface area for oxygen reduction. Nat Mater 2021;20:208–13.
[20] Wang M, et al. Impact of catalyst ink dispersing methodology on fuel cell performance using in-situ X-ray scattering. ACS Appl Energy Mater 2019;2:6417–27.
[21] Tuaev X, Rudi S, Petkov V, Hoell A, Strasser P. In situ study of atomic structure transformations of Pt-Ni nanoparticle catalysts during electrochemical potential cycling. ACS Nano 2013;7:5666–74.
[22] St John S, Hu N, Schaefer DW, Angelopoulos AP. Time-resolved, in situ, small- and wide-angle X-ray scattering to monitor Pt nanoparticle structure evolution stabilized by adsorbed SnCl3- ligands during synthesis. J Phys Chem C 2013;117:7924–33.
[23] Schmies H, et al. Impact of carbon support functionalization on the electrochemical stability of Pt fuel cell catalysts. Chem Mater 2018;30:7287–95.
[24] Schröder J, et al. Tracking the catalyst layer depth-dependent electrochemical degradation of a bimodal Pt/C fuel cell catalyst: a combined operando small- and wide-angle X-ray scattering study. ACS Catal 2022;12:2077–85.
[25] Khalakhan I, et al. Evolution of the PtNi bimetallic alloy fuel cell catalyst under simulated operational conditions. ACS Appl Mater Interfaces 2020;12:17602–10.
[26] Bogar M, Khalakhan I, Gambitta A, Yakovlev Y, Amenitsch H. In situ electrochemical grazing incidence small angle X-ray scattering: from the design of an electrochemical cell to an exemplary study of fuel cell catalyst degradation. J Power Sources 2020;477.
[27] Bogar M, et al. Interplay among dealloying, Ostwald ripening, and coalescence in PtXNi100-XBimetallic alloys under fuel-cell-related conditions. ACS Catal 2021;11:11360–70.
[28] Vad T, Haubold H-G, Èfner NW, Ènnemann HB, Katalyse AH. Three-dimensional Pt-nanoparticle networks studied by anomalous small-angle X-ray scattering and X-ray absorption spectroscopy. J Appl Crystallogr 2002;35:459–70.
[29] Larson-smith K, Jackson A, Pozzo DC. Small angle scattering model for Pickering emulsions and raspberry particles. J Colloid Interface Sci 2010;343:36–41.
[30] Sen D, et al. Amphiphilic interaction-mediated ordering of nanoparticles in Pickering emulsion droplets. Soft Matter 2023;19:3953–65.
[31] Rao J, Zhang H, Gaan S, Salentinig S. Self-assembly of polystyrene - b - poly(2-vinylpyridine) micelles: from solutions to silica particles surfaces. 2016. https://doi.org/10.1021/acs.macromol.6b01074.
[32] Gommes CJ, Prieto G, De Jongh PE. Small-angle scattering analysis of empty or loaded hierarchical porous materials. 2016. https://doi.org/10.1021/acs.jpcc.5b09556.
[33] Gommes CJ, Asset T, Drnec J. Small-angle scattering by supported nanoparticles: exact results and useful approximations. J Appl Crystallogr 2019;52:507–19.
[34] Yakovlev YV, et al. Ionomer content effect on charge and gas transport in the cathode catalyst layer of proton-exchange membrane fuel cells. J Power Sources 2021;490.
[35] Yakovlev YV, et al. Characterization of gas diffusion layer transport properties by limiting current approach. Electrochim Acta 2022;404:139755.
[36] Amenitsch H, et al. First performance assessment of the small-angle X-ray scattering beamline at ELETTRA. J Synchrotron Radiat 1998;5:506–8.
[37] Burian M, Meisenbichler C, Naumenko D, Amenitsch H. SAXSDOG: open software for real-time azimuthal integration of 2D scattering images. J Appl Crystallogr 2022;55:677–85.
[38] Binninger T, et al. Particle-support interferences in small-angle X-ray scattering from supported-catalyst materials. Phys Rev Appl 2015;3:1–6.
[39] Yarusso DJ, Cooper SL. Microstructure of ionomers: interpretation of small-angle X-ray scattering data. Macromolecules 1983;16:1871–80.
[40] Armstrong BH. Spectrum line profiles: the Voigt function. J Quant Spectrosc Radiat Transf 1967;7:61–88.
[41] Whiting EE. An empirical approximation to the Voigt profile. J Quant Spectrosc Radiat Transf 1968;8:1379–84.
[42] Drayson SR. Rapid computation of the Voigt profile. J Quant Spectrosc Radiat Transf 1976;16:611–4.
[43] Humlíček J. Optimized computation of the voigt and complex probability functions. J Quant Spectrosc Radiat Transf 1982;27:437–44.
[44] Schreier F. The Voigt and complex error function: a comparison of computational methods. J Quant Spectrosc Radiat Transf 1992;48:743–62.
[45] Debye P, Bueche AM. Scattering by an inhomogeneous solid. J Appl Phys 1949;20:518–25.
[46] Debye P, Anderson HR, Brumberger H. Scattering by an inhomogeneous solid. II. the correlation function and its application. J Appl Phys 1957;28:679–83.
[47] Teixeira J. Small-angle scattering by fractal systems. J Appl Crystallogr 1988;21:781–5.
[48] Schaefer DW, et al. Multilevel structure of reinforcing silica and carbon. J Appl Crystallogr 2000;33:587–91.
[49] Glatter O. Scattering methods and their application in colloid and interface science. Scattering Methods and their Application in Colloid and Interface Science. Elsevier; 2018. https://doi.org/10.1016/c2016-0-04640-5.
[50] Alt K, et al. Self-assembly of oriented antibody-decorated metal–organic framework nanocrystals for active-targeting applications. Adv Mater 2022;34.
[51] Kotlarchyk M, Chen SH. Analysis of small angle neutron scattering spectra from polydisperse interacting colloids. J Chem Phys 1983;79:2461–9.
[52] Kotlarchyk M, Stephens RB, Huang JS. Study of Schultz distribution to model polydispersity of microemulsion droplets. J Phys Chem 1988;92:1533–8.
[53] Smith MC, Gilbert JA, Mawdsley JR, Seifert S, Myers DJ. In situ small-angle X-ray scattering observation of Pt catalyst particle growth during potential cycling. J Am Chem Soc 2008;130:8112–3.
[54] Sorensen CM, Wang GM. Size distribution effect on the power law regime of the structure factor of fractal aggregates. Phys Rev E 1999;60:7143–8.

[55] Gebel G, Diat O. Neutron and X-ray scattering: suitable tools for studying lonomer membranes. Fuel Cell 2005;5:261–76. https://doi.org/10.1002/fuce.200400080.
[56] Xu F, Diat O, Gebel G, Morin A. Determination of transverse water concentration profile through MEA in a fuel cell using neutron scattering. J Electrochem Soc 2007;154:B1389.
[57] Mališ J, et al. Changes in Nafion® 117 internal structure and related properties during exposure to elevated temperature and pressure in an aqueous environment. Electrochim Acta 2018;262:264–75.
[58] Rubatat L, Gebel G, Diat O. Fibrillar structure of Nafion: matching fourier and real space studies of corresponding films and solutions. Macromolecules 2004;37:7772–83.
[59] https://www.fuelcellstore.com/fuel-cell-components/catalyst/platinum-catalysts/40-platinum-carbon-xc-72r.
[60] Slade S, Campbell SA, Ralph TR, Walsh FC. Ionic conductivity of an extruded Nafion 1100 EW series of membranes. J Electrochem Soc 2002;149:A1556–64.
[61] Wang H, Yuan X-Z, Li H. PEM fuel cell diagnostic tools. CRC Press; 2011.
[62] Gilbert JA, et al. In situ anomalous small-angle x-ray scattering studies of platinum nanoparticle fuel cell electrocatalyst degradation. J Am Chem Soc 2012;134:14823–33.
[63] Bullard JW, Jin Q, Snyder KA. How do specific surface area and particle size distribution change when granular media dissolve? Chem Eng J 2021;406.
[64] Tillier J, et al. Electrochemical flow-cell setup for in situ X-ray investigations. II. Cell for SAXS on a multi-purpose laboratory diffractometer. J Electrochem Soc 2016;163:H913–20.